AGU PUBLICATIONS

JGR

Journal of Geophysical Research: Space Physics

RESEARCH ARTICLE
10.1002/2017JA024022

Special Section:
Geospace system responses to the St. Patrick's Day storms in 2013 and 2015

Variation of atmospheric electric field measured at Vostok, Antarctica, during St. Patrick's Day storms on 24th solar cycle

N. Jeni Victor[1], A. V. Frank-Kamenetsky[2], S. Manu[3,4], and C. Panneerselvam[1]

[1]Equatorial Geophysical Research Laboratory, Indian Institute of Geomagnetism, Tirunelveli, India, [2]Arctic and Antarctic Research Institute, St. Petersburg, Russia, [3]Tata Institute of Fundamental Research, Mumbai, India, [4]Now at MES Degree College, Bengaluru, India

Key Points:
- Positive and negative downward coupling
- Long duration of IMF B_z and prolong recovery phase
- Superposed ionospheric potential on Vostok *PG* (near the magnetic pole) is highly effective for a steady flow of IMF

Supporting Information:
- Supporting Information S1
- Figure S1
- Figure S2
- Figure S3

Correspondence to:
N. Jeni Victor,
jenivictor@gmail.com

Citation:
Jeni Victor, N., A. V. Frank-Kamenetsky, S. Manu, and C. Panneerselvam (2017), Variation of atmospheric electric field measured at Vostok, Antarctica, during St. Patrick's Day storms on 24th solar cycle, *J. Geophys. Res. Space Physics*, *122*, 6332–6348, doi:10.1002/2017JA024022.

Received 11 FEB 2017
Accepted 6 JUN 2017
Accepted article online 9 JUN 2017
Published online 27 JUN 2017

Abstract The influence of solar wind-magnetosphere interaction on the atmospheric electric field is investigated in connection with the two severe geomagnetic storms during 24th solar cycle. The observation was carried out at Vostok (78°27′S, 106°52′E), Antarctica, during 17–18 March 2013 and 17–18 March 2015. Two consecutive substorms were observed at Vostok during the main phase of geomagnetic storms, where the disturbed ionospheric current is antisunward in the morning sector (~04:00–10:00 UT) and sunward in the noon-afternoon sector (~11:00–16:00 UT). Interplanetary magnetic field (IMF) and solar wind interaction enhance the ionospheric potential, which in turn couple with Potential Gradient (*PG*) measured at ground level. Eventually, for the first time, the slope of ~1.0 Vm^{-1} per kV has been demonstrated between Vostok *PG* and overhead ionospheric potential (Weimer_05) during intense ($Kp = 8$) geomagnetic perturbation. The linear relation between *PG* and overhead potential is highly significant on positive coupling, i.e., positive ΔPG changes, whereas the offset of ~25 V/m has been estimated with negative coupling. Ionospheric convection map from Super Dual Auroral Radar Network is more compatible with *PG* on positive coupling, and for negative changes of *PG*, radar observation is more consistent than the Weimer_05 model. Ionospheric electric potential from radar observation and empirical model is highly compromised when a polar cap is dominated by a single negative potential region associated with IMF $B_y \ll 0$. It is inferred that superposed overhead ionospheric potential on Vostok *PG* is highly effective when IMF maintained a steady flow, whereas it is less significance for rapid changes of solar wind-IMF parameters.

1. Introduction

The concept of Global Electric Circuit (GEC) was introduced by *Wilson* [1925]. According to his hypothesis, the thunderstorm activity which occurs mostly in lower latitudes acts as the main source of the electric field in near-Earth surface, where the current flows upward to the ionosphere and completes the circuit flowing downward in fair weather regions to the Earth's surface. This maintains a potential difference of about ~250 kV between the ionosphere and Earth's surface [*Alderman and Williams*, 1996; *Markson*, 2007; *Rycroft and Harrison*, 2011; *Rycroft et al*., 2012], which is commonly measured as surface electric field or Potential Gradient (*PG*) that varies around 130 V/m in fair weather with suitable electric field probes. The thunderstorm generator is mainly dominated in the low-latitude regions, and later two generators were proposed by *Roble and Tzur* [1986], the solar wind-magnetosphere dynamo and ionosphere dynamo (tides) are active in high latitudes (>60°latitude) [*Tinsley*, 2000]. Tides generated in ionosphere causes a horizontal electric potential difference of about 5–15 kV between the low-latitude ionosphere to high-latitude ionosphere [*Richmond*, 1986]. The interaction of the solar wind plasma with the Earth's magnetosphere produces electric fields and currents, which will map to the polar ionosphere along the magnetospheric equipotential lines. This coupling introduces an additional ionospheric potential drop between dawn and dusk. The additional electric field at the ionospheric origin successfully maps down to the lower atmosphere. These three generators can change the amplitude of diurnal variation which depends on the geographical location and time [*Tinsley and Heelis*, 1993; *Michnowski*, 1998]. The long-term and continuous measurement of the atmospheric electric field in high latitudes may contribute to a better understanding of the response of global distribution of the thunderstorm generated electric field and current to solar wind in different time scales [*Aruliah et al*., 1996; *Michnowski*, 1998].

At high latitude, the atmospheric electric field has two components. (1) The potential due to thunderstorm activity (Φ_{int}) around the globe and (2) potential from magnetospheric voltage source (Φ_{ext}). The later

current system establishes the global two-cell convection pattern at ionospheric altitude over the geomagnetic poles directed opposite to each other. The foci of the two cells are in the dawn and dusk sectors of the magnetic local time (MLT) at geomagnetic latitude of approximately 75°. This generates a horizontal dawn-dusk potential drop of 30–150 kV across magnetic conjugate polar caps, with an associated current system of the order of mega amperes. The magnetospheric convection pattern is sun aligned and remains fixed, as Earth rotates on its geographic pole, the pattern moves in a complex style over the Earth's surface. There is a considerable large variation of Φ_{ext} values with time and space when compared with Φ_{int}. This large temporal-spatial variation of Φ_{ext} is due to electric fields of magnetospheric origin which is controlled by the solar wind and ionospheric conductivity. The large-scale horizontal ionospheric electric fields generated by solar wind-magnetosphere dynamo maps down to the ionosphere and to the lower atmosphere were studied as a mapping problem by many researchers using different cases and approaches (to mention a few) [*Böstrom and Fahleson*, 1977; *Park*, 1976; *Roble and Hays*, 1979; *Roble and Tzur*, 1986; *Sheftel et al*., 1994]. According to the mapping problem, the horizontal ionospheric potential due to dawn and dusk would be superimposed on diurnal variations of potential difference between the Earth and the ionosphere. This large-scale potential difference is mapped downward and is transformed to a vertical electric field near the surface which is added characterizes of GEC and depends on interplanetary magnetic field (IMF) and solar wind (SW) parameters. *Park* [1976] and *Roble and Hays* [1979] calculated the perturbations of magnetospheric dynamo on GEC parameters can be ±20% at high latitudes. Later, *Tinsley et al.* [1998] quantitatively reported the significant association between the large-scale ionospheric potential and *PG* measurement at South Pole. He further added, finding the exact link might be difficult due to the indistinguishable effect of local factors on *PG* measurements.

Several studies have been devoted for analyzing *PG* variation during magnetically disturbed periods [*Apsen et al*., 1988; *Michnowski*, 1991] at middle-high latitude [*Belova et al*., 2001; *Kleimenova et al*., 2006, 2010], high-latitude nearly conjugate stations [*Frank-Kamenetsky et al*., 2001, 2012], and auroral region [*Nikiforova et al*., 2003; *Kozyreva et al*., 2007; *Victor et al*., 2016]. There are few cases reported on the modulation of potential gradient by the IMF components (B_z and B_y) [*Michnowski*, 1998; *Frank-Kamenetsky et al*., 2001] and field-aligned currents [*Michnowski*, 1998; *Morozov and Troshichev*, 2008]. In this series, few researchers reported the relation between the variation of *PG* and the overhead ionospheric potential with respect to different location [*Tinsley et al*., 1998; *Corney et al*., 2003; *Kruglov et al*., 2010, and reference therein]. The variation in the *PG* at Vostok which is close to the polar cap is highly influenced by the IMF and overhead ionospheric potential [*Corney et al*., 2003; *Burns et al*., 2005; *Kruglov et al*., 2010; *Odzimek et al*., 2011]. But most of the aforesaid work leads to the climatology of given problems rather than concentrating on the individual events. In which, *Victor et al.* [2016] discussed the departure of the *PG* during three consecutive substorms followed by the severe geomagnetic storm ($Kp > 7$) from network of observation at Antarctica. They observed that the departure of *PG* to that of its quiet time pattern is due to the superposition of polar cap potential and suggested the link is highly pronounced on the polar cap region. However, the influence of solar wind-driven ionospheric potential on *PG* in accordance by temporal and spatial distribution of large-scale ionospheric electric field during intense geomagnetic perturbation elsewhere reported.

It is expected that the result of subtraction of perturbed *PG* from quiet time *PG* has similar pattern with ionospheric potential above at any specified point [*Tinsley et al*., 1998]. But to obtain a distinct dependence of the above two parameters are quite cumbersome, due to the fact that day-to-day variability of the thunderstorm dynamo and precise determination of overhead ionospheric potential, which constantly varies with IMF. In addition, the influence of large-scale ionospheric potential on the *PG* is more complex when the large set of data is handled, because the dawn-dusk potential asymmetry highly varies with IMF structure, season, and magnetic local time (MLT). Therefore, its relation on *PG* may lead to a lack of significant correlation in the spatial and temporal distributions [*Ptitsyna et al*., 1997]. So it is necessary to profoundly investigate by treating each sample as a single entity to find out the complexity involving in this process. This ideology helps to find out any biasing on this solar-terrestrial relation with respect to geographical-magnetic position of measuring sites, season, orography, etc.; this method of analysis is strongly suggested by *Michnowski et al.* [2014]. In this scenario, it is essential to investigate the *PG* variation during strong geomagnetic perturbations at high latitude by means of the influence of solar wind-magnetosphere interaction.

In this study, we present the variation of *PG* measured at Vostok, Antarctic, plateau during St. Patrick's Day storms on 17–18 March 2013 and 17–18 March 2015. The observations aim to investigate the *PG* changes,

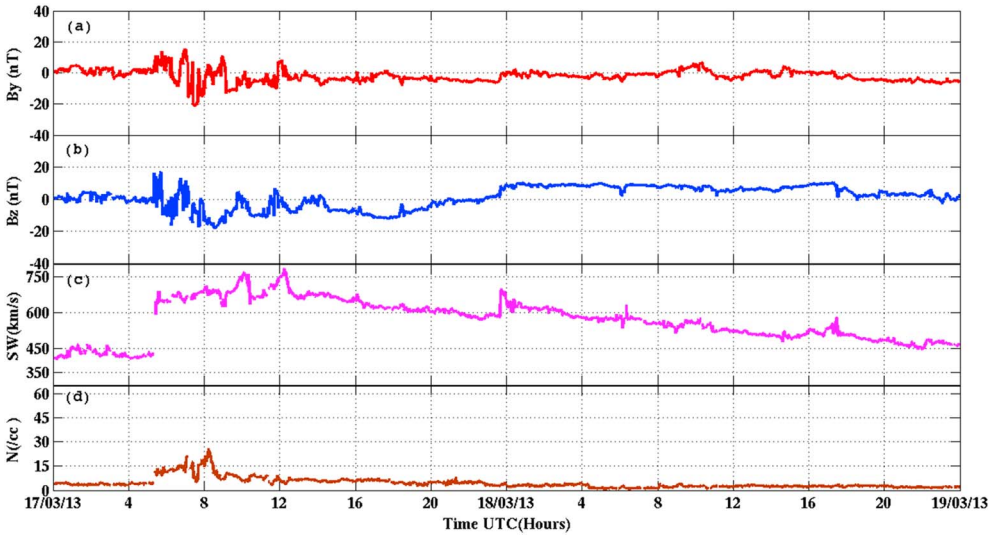

Figure 1. Temporal variation of solar wind-interplanetary magnetic field (SW-IMF) parameters during 17–18 March 2013. (a) IMF B_y (east-west), (b) IMF B_z (north-south) (c) SW (solar wind speed), and (d) N (plasma density).

mostly influenced by the solar wind-magnetospheric generator, during two large geomagnetic perturbations (*Kp* = 8). Tempo-spatial distribution of polar cap potential over Southern Hemisphere and overhead potential at Vostok were obtained from Super Dual Auroral Radar Network (SuperDARN) radar and Weimer_05 model, respectively.

2. Observations

2.1. Characteristics of Storm on 17–18 March 2013

A G3-Class (*Kp* = 7) Earth-directed Coronal Mass Ejection (CME) event has been observed on 17 March 2013, which is one of the strongest geomagnetic disturbances recorded during the 24th solar cycle. It was associated with M1.1 type solar flare from the sunspot 1692 on 15 March 2013 at 07:00 UT. The modulation of solar wind (SW) and interplanetary magnetic field (IMF) high-resolution (1 min) data were obtained from OMNI database (http://omniweb.gsfc.nasa.gov/ftpbrowser/wind_min_merge.html). Planetary indices such as Symmetric *H* (*SYM-H*), *Kp* index, and Auroral indices (*AL*, *AU*) were obtained from WDC, Kyoto (http://wdc.kugi.kyoto-u.ac.jp/). Temporal variation of SW-IMF parameters during 17–18 March 2013 is depicted in Figure 1. The incoming CME enhances the IMF B_z (north-south) to strong northward and solar wind speed raised to 600 km/s at 05:30 UT on 17 March 2013, while density and IMF B_y (east-west) also significantly vary. Temporal variation of planetary indices and Vostok *PG* variation on 17–18 March 2013 are shown in Figure 2. The enhanced ram pressure because of density hitting on magnetosphere triggers the magnetopause current, which enhances our terrestrial magnetic field, which is registered as a sudden storm commencement (SSC) on *SYM-H* as shown in Figure 2b. The main phase of the magnetic storm onset observed near 06:00 UT was associated with the strong southward IMF. The fast stream of incoming solar wind particles enters the high-latitude ionosphere and changes its conductivity and electric field. Its equivalent current leaves a signature in ground magnetic field component as a positive enhancement of ΔH by 450 nT and ΔZ by −300 nT measured at Vostok at about 08:00 UT as shown in Figure 2d; it implies the intensification of anti-sunward ionospheric current during strong IMF southward ($B_z = -17$ nT).

From Figure 1b, three consecutive phase reversals of IMF B_z from strong south to north are observed at 08:30 UT, 11:00 UT, and around 13:00 UT. The first enhancement at 08:30 UT ($B_z = -19$ nT) corresponds to a sudden blast of particle density (>20/cm^3) and high-speed solar wind plasma as seen in time series. Simultaneously, the sunward polar cap current is inferred as a negative trend in ΔH, which is followed by an enhancement of *AL* (−1000 nT) and *Kp* = 7. The second enhancement (11:00 UT) is associated by westward (dawnward) (IMF $B_y < 0$) flow of IMF with increasing speed and mean density (8/cm^3). On this period, the enhanced plasma motion by the solar wind speed intensifies the prevailing ionospheric current over Vostok. The final phase

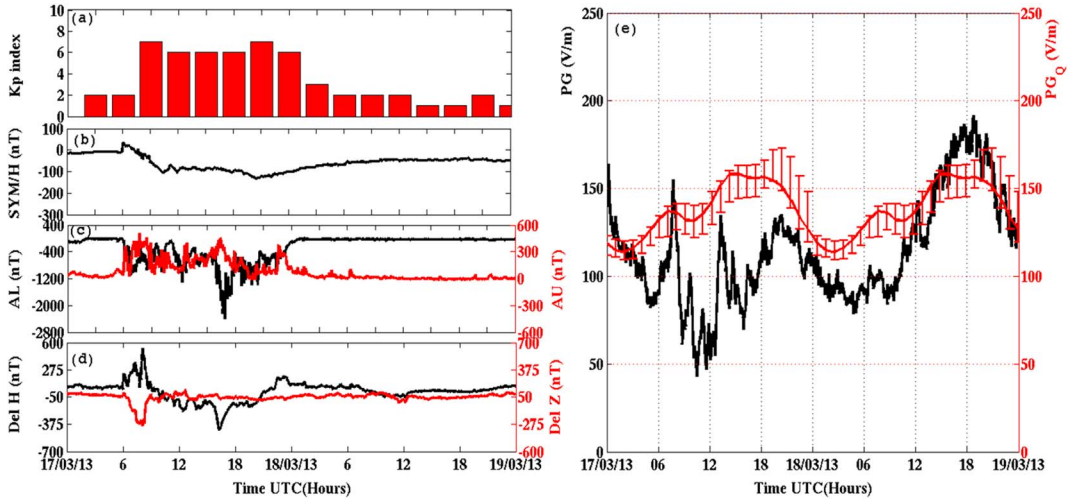

Figure 2. Temporal variation of planetary indices and Vostok *PG* variation on 17–18 March 2013. (a) *Kp* index, (b) Symmetric-*H*, (c) Auroral Lower (*AL*) and Auroral Upper (*AU*), (d) ΔH and ΔZ measured at Vostok, and (e) *PG* and PGQ (Quiet time curve) from Vostok.

enhancement (13:00 UT) corresponds to the considerable changes in B_z (−10 nT) and B_y (−10 nT) and does not make an impact on the magnetic field variation at Vostok; however, *AL* shows a strong enhancement (−1500 nT) during 12:00–13:00 UT. On an average, north-south (B_z) component of IMF varied from +15 nT to −20 nT and east-west (B_y) component of IMF varied from +13 nT to −20 nT during the initial course of study. The IMF fluctuations, as seen in Figures 1a and 1b, seem to be due to the turbulent motion of incoming solar wind plasma.

During the main phase of *SYM-H*, 15:00–18:00 UT, the sunward current substantially decreases the ΔH (−450 nT) at Vostok (magnetic) latitude followed by an increase in *AL* index by −2000 nT as depicted in Figure 2, which is the strongest auroral current occurred during the entire course of time. The maximum magnetic deviation observed on *SYM-H* is −137 nT at 20:00 UT, where *Kp* persisted between 6 and 7. The recovery phase of the geomagnetic storm started at 20:00 UT, and then *SYM-H* gradually increases to −50 nT at 09:00 UT on 18 March as depicted in Figure 2b. The prolonged recovery phase is almost sustained for more than 4 days, varying −50 nT from the time of SSC.

2.2. Characteristics of Storm on 17–18 March 2015

The magnetic filament eruption from sunspot AR2297 on the Sun during early hours of 15 March 2015 propelled a CME, which has reached the bow shock nose around 04:00 UT and hit the Earth's magnetosphere around 04:30 UT on 17 March 2015. Temporal variation of solar wind and IMF parameters during 17–18 March 2015 is depicted in Figure 3. During morning hours of the day on 16 March, the density fluctuation between 15 and 35/cm^3 is highly disturbed, and IMF components vary ±10 nT. This stormy behavior tends to be minimal in the evening sectors to the midnight hours. Shortly after, around 05:00–06:00 UT IMF B_z magnitude intensified to −20 nT, while IMF B_y has significantly changed by −20 nT. Three-hourly index of *Kp* and hourly variations of *SYM-H*, *AL* and *AU*, and Digital Fluxgate Magnetometer (DFM) variations from Vostok on 17–18 March 2015 are depicted in Figure 4. The main phase of the storm started around 05:00 UT associated with IMF *Bz* southward, which causes the negative excursion on *SYM-H* as shown in Figure 4b. Simultaneously, during the growth phase of the substorm, disturbed polar ionospheric current develops and its equivalent convection electric field extends to lower latitudes. The intensity of its equivalent current registered in ΔH at Vostok as a positive trend of 400 nT at 06:00 UT as presented in Figure 4d. The IMF B_z phase reversal is observed from 05:30 UT to 06:00 UT, whereas IMF B_y is sustained on the same phase, westward. This small-scale phase reversal of B_z has consecutively occurred for every half an hour interval from 06:00 to 13:00 UT, while plasma density and solar wind speed were considerably high.

Other than the small-scale changes of IMF B_z, three distinct changes of the field were also noticed at 08:00 UT, 11:00 UT, and 13:00 UT as inferred from Figure 3b. The strong IMF south phase turned to the north around

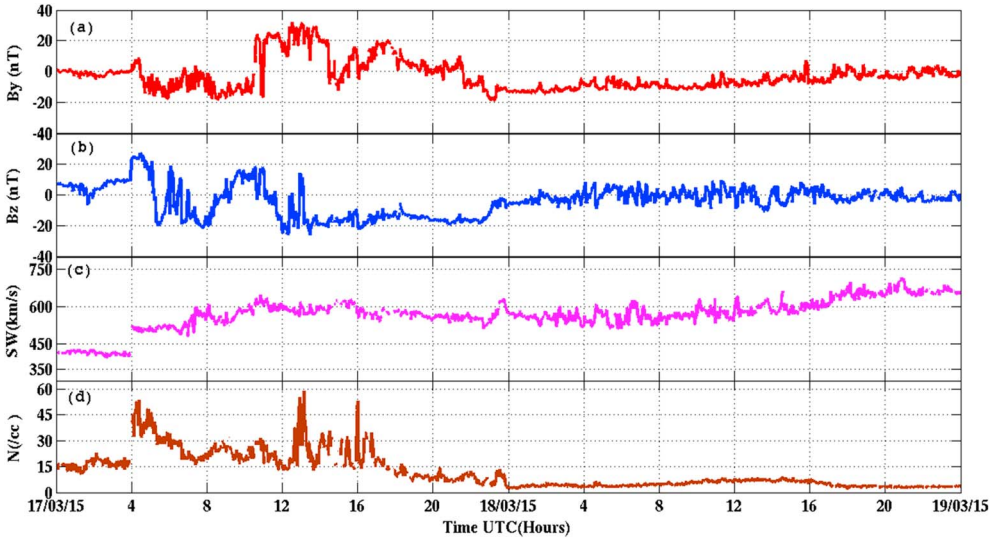

Figure 3. Temporal variation of SW-IMF parameters during 17–18 March 2015. (a) IMF B_y (east-west), (b) IMF B_z (north-south), (c) SW (solar wind speed), and (d) N (plasma density).

08:00 UT, and it is further strengthening in the same direction, +12 nT, at 10:00 UT. This 2 h positive excursion covers almost 35 nT of B_z variation (−20 to +15 nT), where B_y remains westward. It can be noted from Figures 3a and 3b around 10:30 UT, IMF simultaneously changes its phases as B_y turned to east, and B_z dropped to southward for a span of 10–20 min. From 11:00 UT, B_z again turned south and remained until next day; however, there is two short-term (10–20 min) phase reversals occurred between 12:00 and 13:00 UT. IMF B_y remains stable toward east (~30 nT) for more than 3 h (11:00–14:30 UT) and a large density blast ($N_{sw} > 50/cm^3$) occurred at 13:00 UT as shown in Figures 3a and 3d. Notably, solar wind drifts with high speed along with strong southward directing IMF during this period. As an effect, the flow of newly opened magnetic field lines from magnetic dayside are directed toward dusk because of strong dawn-dusk flow ($B_y > 0$) [e.g., *Galperin et al.*, 1978; *Heelis*, 1978]. In this situation, an intensification of equivalent polar cap current substantially decreases the ΔH of −500 nT as shown in Figure 4. It is to be noticed from Figure 4c, *AL* is extremely increased by −2000 nT and is associated with the huge density fluctuation occurred around 13:00 UT. A long main phase and prolonged recovery phase of the geomagnetic storm were witnessed from *SYM-H*, where the intense magnetic disturbance of −233 nT is noticed at 23:00 UT. The onset of G3/G4, particularly G4 at 14:00 UT, was due to prolonged planetary index value at 7 and 8 for

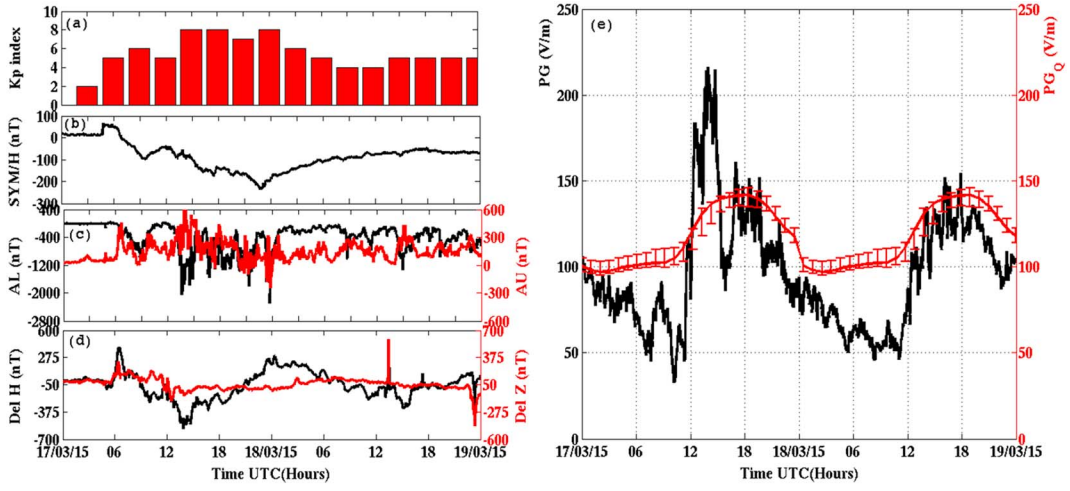

Figure 4. Temporal variation of planetary indices and Vostok *PG* variation on 17–18 March 2015. The panels are same fashion as Figure 2.

several hours (Kp = 8, at 12:00–15:00) associated with sudden increase in solar density with strong IMF prevailing southward at 13:00 UT.

The salient features of St. Patrick's day storm on 17 March 2015 is that (a) IMF B_z drastically changes from +30 to −30 nT (~−60 nT) in a day, (b) IMF southward phase has prolonged for more than 12 h during the main phase of the storm, (c) solar wind density enormously increases in three consecutive periods (>50/cm^3, third is at 16:00 UT) by tenfold higher than quiet time values (5/cm^3), (d) particle density is sustained at 20/cm^3 for almost ~13 h, when IMF B_z has prolonged south phase, and (e) Kp index is sustained at 7–8 (G3/G4) roughly for 12 h.

2.3. *PG* Observation at Vostok, Antarctica

PG measured at Vostok during 17–18 March 2013 and 17–18 March 2015 has been investigated in this study. These two geomagnetic storms have similar main phases and a long journey of recovery phases (almost 72 h *SYM-H* < −40 nT) which make this space weather event more important. Moreover, it is one of the unique observations to discuss the large geomagnetic storm over Vostok using *PG* measurement.

For any particular event, the electrical coupling would be much complicated, and hence, it is necessary to take into account the position of the measuring site with respect to the thunderstorm generators and determine the course of daily global thunderstorm electric field which may even differ from the Carnegie curve [*Burns et al*., 2005]. For the construction of the undisturbed variation of *PG* (i.e., PGQ), fair weather [*Frank-Kamenetsky et al*., 2001] days from March 2013 (14 days) and 2015 (13 days) were selected. One minute resolution data were used for smoothing and detrending by Gaussian kernels method [*Kantelhardt et al*., 2002].

2.3.1. 17–18 March 2013

Five min averaged *PG* along with PGQ is depicted on an hourly scale on 17–18 March 2013 in Figure 2e. To speculate the changes in *PG* due to magnetic perturbation, the quiet time fair weather pattern (PGQ) is overplotted in the same figure. Diurnal pattern of *PG* shows similar pattern as PGQ; however, the departure of *PG* values from the quiet curve distinctly represents the modulation of field by the external sources. Similarly, the variance of *PG* from PGQ periods mostly coincides with the period of magnetic perturbation. It can be seen from the meteorological variation that the local factors have negligible influences on *PG* measurement (Appendix-I). The difference between *PG* and PGQ is considerably high when the polar cap current was intensified over Vostok. It is inferred that substorm can significantly modulate the *PG* by changing the electrodynamics of the ionosphere, which is the part of the global electric circuit [*Kleimenova et al*., 2013]. From 06:00 UT, the considerable changes on *PG* are noticed, in which, the negative excursion (relative to the PGQ) is initiated from 07:00 UT, where the strong ΔH perturbation is found at Vostok. The extended *PG* negative bay of ~50 V/m remained active up to 13:00 UT. *PG* variation due to the magnetic perturbation is gradually recovered after 18:00 UT when the Kp index decreased. The amplitude of *PG* varied as high as 150 V/m and lower as 45 V/m with the daily average of 105 V/m, whereas PGQ has average of 138 V/m. The next consecutive day, *PG* depicts the typical fair weather pattern with PGQ as shown in Figure 2e.

2.3.2. 17–18 March 2015

Temporal variation of Vostok *PG* on 17–18 March 2015 is shown in Figure 4e and Vostok PGQ; fair weather pattern is overplotted to compare the differential pattern (same fashion as Figure 2e). In midnight sector, *PG* follows the PGQ and the significant difference appears from 06:00 UT, where the magnetic activity triggered over Vostok due to the southward turning of IMF, while ΔH shows an intensification of antisunward polar cap current as shown in Figure 4d. Its equivalent large-scale horizontal ionospheric electric field significantly influences the *PG* by decreasing its magnitude to ~50 V/m during 07:00–08:00 UT, which is well below PGQ values for that UT hour. The negative trend of *PG* (relative to PGQ) continues till 12:00 UT; later, it is substantially increased to well above PGQ at 210 V/m. In this interval, a strong duskward motion is inferred from IMF B_y and its equivalent current substantially decreased ΔH, as large negative bay, at Vostok, is noticed in Figure 4c. In addition, the Kp index is also increased to 8 and sustained for further 09 h. *PG* gradually dropped from its maximum departure at 14:00 UT; shortly after, it reached well below the PGQ as seen in Figure 4e. From 17:00 UT, *PG* increased of approaching PGQ pattern, but it is noticed that the geomagnetic storm is still progressing (Kp = 8). Similar to an earlier event, the *PG* variation on poststorm day follows PGQ.

2.4. Ionospheric Potential

In the context of dawn-dusk potential variation, there are recent models quantitatively describe the changes of ionospheric potential over high latitude [*Rich and Hairston*, 1994; *Papitashvili et al*., 1994; *Boyle et al*., 1997]

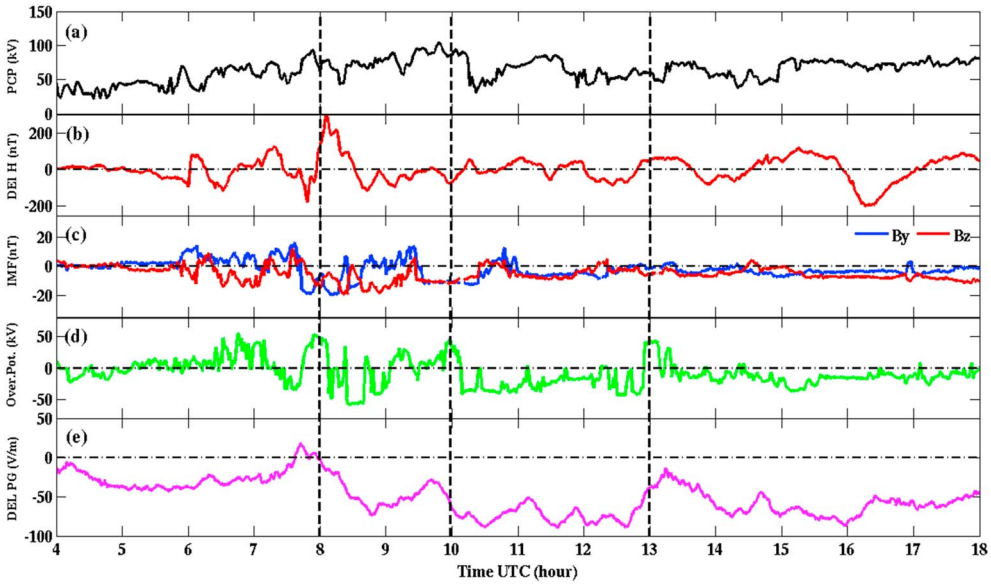

Figure 5. Hourly variation of PCP, RSD of ΔH, IMF, overhead potential (Weimer05), and ΔPG variation during 04:00–18:00 UT on 17 March 2013. (a) PCP, (b) RSD (ΔH), (c) IMF (B_y and B_z), (d) overhead potential, and (e) ΔPG. The dashed lines specified the intervals where ΔPG significantly influenced by ionospheric potential.

and estimated from satellite [*Weimer*, 2000], radar observation technique (SuperDARN) [*Ruohoniemi and Greenwald*, 2005]. These models are constructed based on the interaction of solar wind-IMF parameters since the ionospheric horizontal electric field is basically driven by them.

We have obtained ionospheric electric potential above Vostok (magnetic latitude 83.6°S) with 1 min time resolution from the Weimer_05 model. The model output requires corrected geomagnetic coordinates (CGM) of the given location, solar wind speed, number density, IMF (B_y and B_z) parameters, and corresponding date, hour to calculate dipole tilt angle [*Weimer*, 2005a, 2005b]. A time delay is applicable between model-calculated solar wind-imposed ionospheric potential and Vostok *PG* measurement, as detailed in *Burns et al.* [2012], which is approximately 60 min, including the time taken between the incoming solar wind at the magnetopause and its plasma flow response in the polar ionosphere [*Hairston and Heelis*, 1995; *Weimer*, 2001], initiation of plasma flow response in the polar ionosphere and to complete the plasma flow realignment [*Ridley et al*., 1998], and finally *PG* changes for the polar ionospheric convection [*Bering et al*., 1998].

From the standpoint of direct observations of horizontal ionospheric electric field, the time series of polar cap potential (PCP) and its associated convection pattern (http://vt.superdarn.org/tiki-index.php?page=map+summary+plots) were obtained from the SuperDARN radar system covering the high-latitude regions of the Southern (8 radars) and Northern (12 radars) Hemisphere. The coherent scatter radars are operated at high-frequency band (8–20 MHz), and combining the line-of-sight vectors from these radars with overlapping field of view can provide over larger area giving a comprehensive view of plasma motion in the polar ionosphere. PCP varies from 10 to 20 kV under magnetically quiet conditions to 50–120 kV during magnetically disturbed condition [*Morozov and Troshichev*, 2008]. The high-resolution ionospheric convection map and PCP data are available for every 2 min interval with a spatial resolution of 1° in latitude and 2° in longitude. Figure 5 shows the temporal variation of PCP, overhead potential (Weimer _05 model), ΔPG, RSD (root-mean-square deviation) of ΔH and IMF parameters on 17 March 2013. Figure mainly focuses on the onset of magnetic storm from morning sector to evening sector (~04:00 UT–18:00 UT). The measured *PG* over high latitude is composed of global thunderstorm-generated electric field (PGQ) and overhead ionospheric potential (PG_{ext}) due to solar wind-magnetospheric interaction [*Richmond*, 1986; *Tinsley*, 2000; *Kruglov et al*., 2010]. These two components are embedded with the regression coefficient (α), which is linearly proportional to columnar conductivity at the station [*Frank-Kamenetsky et al*., 2012]. Hence, it is necessary to speculate their independent contributions, so that the PG_{ext} would be merely attributed to external magnetospheric generator. The PG_{ext} (ΔPG) is estimated by the given equation.

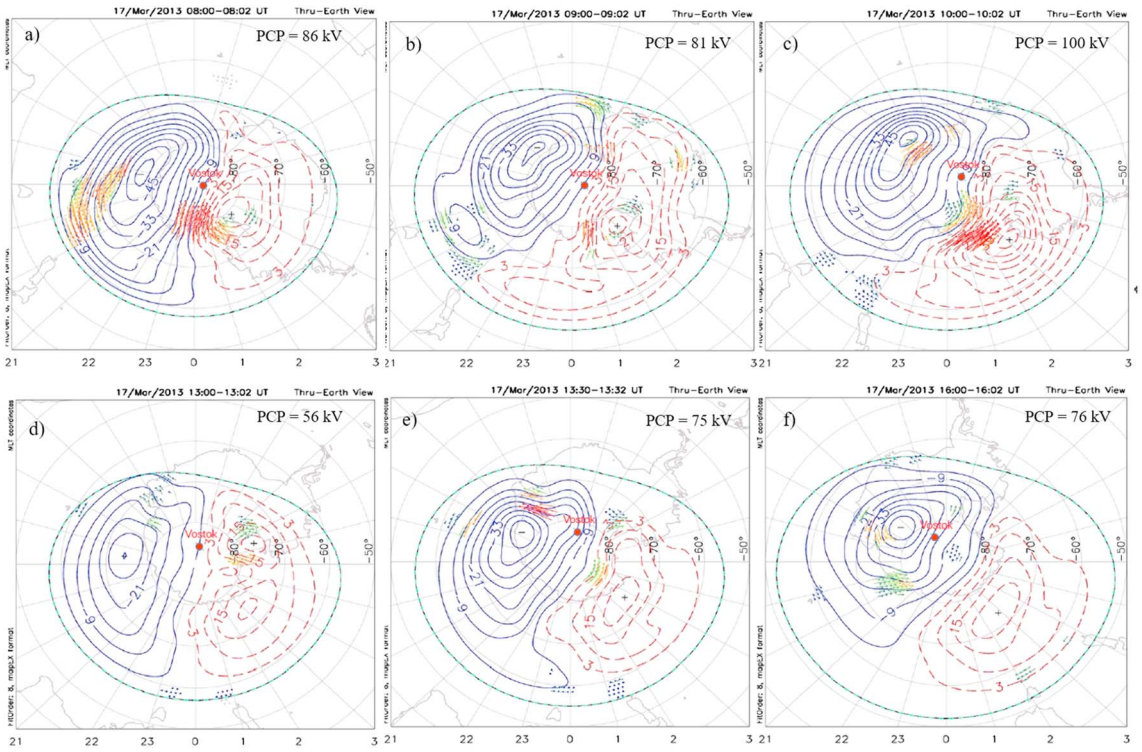

Figure 6. Two-cell ionospheric convection maps obtained from SuperDARN observation on 17 March 2013 for the period of disturbances. The location of the Vostok is marked as red dot on the map.

$$\Delta PG\ (\mathrm{h}) = PG\ (\mathrm{h})\ (\mathrm{Vostok}) - \mathrm{PGQ}\ (\mathrm{h})\ (\mathrm{reference\ curve} - \mathrm{Vostok})$$

In Figure 5d, the time shift (~60 min) between ionospheric potential and ΔPG is applied. The vertical dashed lines denote the time of transition state of ΔPG associated with ionospheric potential, where the first two lines indicate the negative transition and last one is for positive transition.

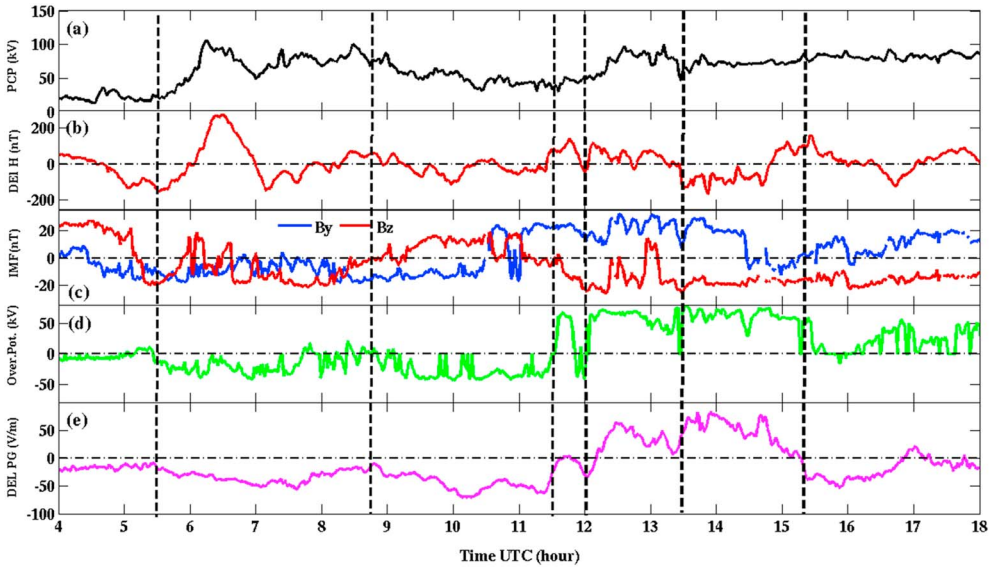

Figure 7. Hourly variation of PCP, RSD of ΔH, IMF, overhead potential (Weimer_05), and ΔPG variation during 04:00–18:00 UT on 17 March 2015. (a) PCP, (b) RSD (ΔH), (c) IMF (B_y and B_z), (d) overhead potential, and (e) ΔPG. The dashed lines specified the intervals where ΔPG significantly influenced by ionospheric potential.

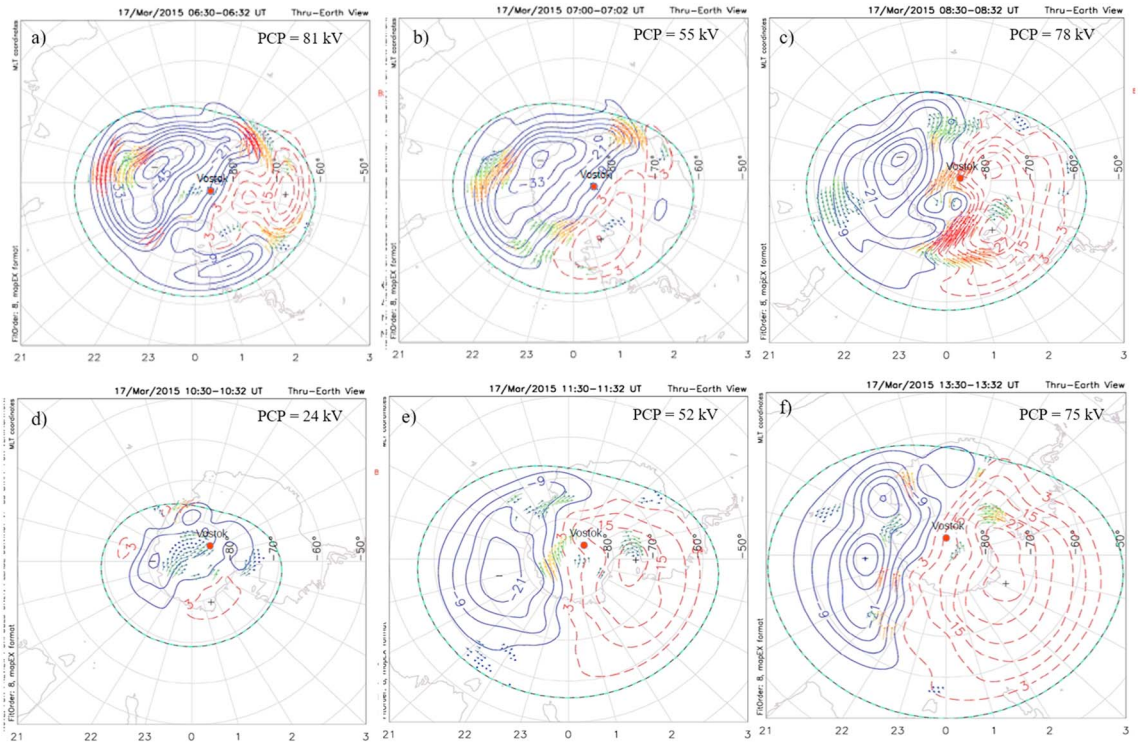

Figure 8. Ionospheric plasma convection maps in the high-latitude region on 17 March 2015. (a–f) Different time intervals are given at the top of each panel.

The thru-Earth view of two-cell convection maps obtained from SuperDARN over Southern Hemisphere is presented in Figure 6. The "blue" contour lines and "red" dotted lines illustrate the negative and positive potential region, respectively, and the Vostok is indicated by a "red" dot on each convection maps. The corresponding polar cap potential drop is given in the top right corner of each convection maps. In a similar fashion, Figure 7 shows PCP, overhead potential at Vostok, ΔPG, RSD of ΔH, and IMF variation during 04:00–18:00 UT on 17 March 2015. Time series of ionospheric potential plotted in Figure 7d is post shifted by 1 h to equate the ΔPG changes. First and last three dashed lines cover the negative and positive transition of ΔPG, respectively. Figure 8 depicts the ionospheric convection maps obtained from the SuperDARN observation for different interval from 06:30 UT to 13:30 UT on 17 March 2015.

3. Discussion

We have presented the variation of Vostok *PG* during two severe geomagnetic storms on 17–18 March 2013, 2015 during 24 solar cycle. The later storm is more severe (*SYM-H* −233 nT) than former (*SYM-H* −132 nT). As described in the above sections, the second storm has salient features than the first one by many aspects such as the strength of the storm (*Dst*), duration of stable IMF, and SW parameters, they play a crucial role in solar wind-magnetosphere-ionosphere coupling. However, two events have similarities like, both are flare associated CMEs, a similar period of main phase (~18 h), and long recovery phase (more than 72 h). The high-latitude upper atmosphere is quite sensitive to the solar wind-magnetosphere interaction. During the main phase of intense geomagnetic storm, the effects on high-latitude ionosphere are highly pronounced [*Kleimenova et al*., 2012, 2013].

In general, diurnal variation of *PG* is highly sensitive to seasonal changes and varies significantly with each season because of the seasonal variability of lightning activity over the globe [*Kleimenova et al*., 2013]. The present data set avoids such seasonal biasing on the *PG* measurement, since the event days fall on the same, autumn (March, April, and May), season of the Antarctica Plateau. Temporal variation of automatic weather station parameters shows that the days are fair weather, followed *Frank-Kamenetsky et al.* [2001] criteria, and so the influence of local meteorological factors on *PG* during given period is negligible.

The magnetic storm main phase is commonly accompanied with a high-latitude substorms, which is synchronized with precipitation of energetic electrons in the night sectors. As a result, the intense magnetospheric and ionospheric disturbances are observed during the magnetic storm main phase, and it is anticipated to modulate the *PG* measured above 60° latitude. As shown in Figure 5a, PCP gradually varies from 05:00 UT associated with the south-west turning of IMF, and similar increasing trend is observed on overhead ionospheric potential as seen in Figure 5d. The incoming solar wind plasma interacts with magnetosphere by enhancing particle precipitation at high-latitude upper atmosphere; it intensifies the ionospheric potential over the polar cap which influences the *PG* from 06:00 UT on 17 March 2013. The strong southward IMF ($B_z < -18$ nT) occurred during 07:00–08:00 UT enhances the dayside magnetic field merging efficiency between IMF and northward geomagnetic field. The coupling function ($VB\sin\theta$, where θ is IMF clock angle) parameterizes the ionospheric convection electric field, which is the measurement of rate of magnetic flux transfer from solar wind to the magnetosphere-ionosphere system [*Gao et al*., 2013]. It accounts the increase in overhead potential above Vostok and PCP by 50 kV and 90 kV at 08:00 UT. As proposed [*Park*, 1976; *Roble and Hays*, 1979], the increased ionospheric potential significantly alters the *PG* by 60 V/m at Vostok. It is inferred from IMF, under negative B_y (20 nT) the open field lines at polar cap are pulled westward and added to the dawnside of the southern polar cap [*Khan and Cowley*, 2001]; hence, the flow from dusk to dawn expands the negative potential region. Simultaneously, ΔPG decreased by 75 V/m during 08:00–09:00 UT caused by sharp negative changes of overhead ionospheric potential ~−58 kV, while PCP also increased up to 75 kV. It can be observed from Figure 6a that the two cells bisect polar cap almost equally where Vostok falls in the negative potential region at 08:00 UT, when ΔPG substantially decreased. *Apsen et al.* [1988] and *Kleimenova et al.* [2010] reported that negative *PG* deviation is accompanied with negative potential region dominating over the location. It is generalized with the assumption that positive *PG* deviation during morning hours may be due to dawn convection cell, and dusk cell corresponds to the negative *PG* deviation during evening hours [*Burns et al*., 2005]. But the system is relatively complex on the polar cap region during geomagnetic disturbances, where the ionosphere-magnetosphere electrodynamics are governed by the open geomagnetic field lines and the system is highly variable for the fluctuating SW-IMF. Figure 6 shows the domination of negative potential region over Southern Hemisphere relative to the Sun position for a different period of interest.

At 08:45 UT, ΔPG is gradually turning to positive phase for an hour, where negative potential region slowly moves away from Vostok as shown in Figure 6b. When IMF B_y turned positive as shown in Figure 5c, i.e., the field lines gradually change its direction to duskside, so the positive potential region expands while the negative potential region compressed. One can see from Figure 5d, overhead potential highly fluctuates between positive and negative due to the rapid changes of IMF, and mapping of such fast-varying potential may lead to poor correlation with ground measured *PG*. Later, ΔPG encounters a sharp magnitude drop from ~09:45 UT to 11:00 UT by −88 V/m, which is one of the lowest ΔPG values observed on 17 March 2013. Simultaneously, PCP shows very high amplitude ~98 kV due to the net effect of high-speed solar wind plasma (V_{sw} = 750 km/s) along with strong southward IMF. As seen from Figure 6c at 10:00 UT, the negative potential region extended its limbs above Vostok and entirely dominated. As a result, the overhead potential efficiently maps down and leads for the decrement of ΔPG. The linear relation between overhead ionospheric potential obtained from IZMIRAN Electrodynamic Model and Vostok PG was estimated by *Frank-Kamenetsky et al.* [1999], and later extensive study was done with a large set of data using ionospheric model Weimer_96 by *Burns et al.* [2005]. *Burns et al.* [2012] further improved the relation with the aid of improved Weimer_2001. The slope of the relation from the above analysis is determined from 0.7 to 0.806 ± 0.06 Vm^{-1} kV^{-1}, and the consistency between the studies had discerned.

From 10:00 UT to 13:00 UT, ΔPG shows large negative excursion >−60 V/m of having three up and down (<−50 V/m) trends as shown in Figure 5e. It is evident from Figure 5d, the overhead potential distinctly shows a similar pattern of variation by −33 kV. During this period, IMF components are not stable and they highly fluctuate because of turbulent motion of plasma, which ultimately controls the convection pattern between dawn and dusk. It is understood, the ionospheric plasma convection pattern is well established for IMF southward, but not well known for a sudden change in the orientation of IMF [*De Michelis et al*., 2016]. Hence, the synoptic snapshot of convection map from SuperDARN is essential to explain the convection pattern changes. In this situation, upward phases of ΔPG are thought to correspond with the movement of convection vortex away from Vostok; on the other hand, it approaches the positive potential region,

further the intensification of negative ΔPG perhaps associated with close vicinity of the negative ionospheric potential region over Vostok. Time series of estimated overhead ionospheric potential and its phase support the domination of respective convection pattern above Vostok. The offset of ~25 V/m has been approximated by ΔPG and Weimer_05 model during this interval.

The gradual increase of ΔPG observed during 12:40–13:10 UT may be associated with inward contraction of the negative potential region due to northward IMF. For example, Figure 6d depicts the distorted two-cell system due to northward turning of IMF at 13:00 UT, and the overhead potential also varies as a sharp increase from negative to a positive potential. The radar observation and modeled potential mutually support the contraction of the ionospheric potential region with respect to Vostok latitude. As Vostok located, almost, at the edge of the negative potential region, the mapping efficiency might also be downsized than earlier hours (at 10:00 UT in Figure 6c). The relaxation time of atmosphere is about of 30–40 min for any ionospheric changes, where the overhead ionospheric potential, modeled, is highly controlled by IMF, which could accommodate the rapid changes of solar wind. However, for any change of IMF, especially northward to southward vice versa, the convection pattern almost takes 4–6 min to alter the pattern [*Hashimoto and Kikuchi*, 2005]. Therefore, when the fast-varying ionospheric potential couples with *PG*, the level of uncertainty in temporal estimation tends to increase. Southward turning IMF again triggers magnetic perturbation at 13:00 UT, which enhances the PCP from 50 to 73 kV. In this interval, overhead potential extends to its negative excursion accompanied with decreasing ΔPG by two levels at 14:00 UT and at 16:00 UT. As observed from Figure 5c, IMF B_y negative phase enhances the dusk to dawn plasma flow and field lines, which strengthens the negative potential region over a positive region. The corresponding ionospheric convection maps have been presented in Figures 6e and 6f, where the Vostok is almost within the area of closely packed negative potential region at 13:30 UT, which owed for changes observed on ΔPG at 14:00 UT. Similarly, the map at 16:00 UT shows the centermost position of Vostok to the negative potential region as observed from Figure 6f. This close vicinity of the negative potential region leads for the substantial decrement of *PG*, which causes the second lowest ΔPG variation (-85 V/m) at Vostok. It is noticed from 13:30 UT to 18:00 UT in the Figure 5e, the ΔPG never attained close to zero level, i.e., fair weather limit, which implies that Vostok was continuously dominated by negative potential region for the entire periods. This inference is highly consistent with the time series of modeled overhead ionospheric potential as in Figure 5d, except the sharp increasing potential caused by the southward and eastward IMF around 13:00 UT. Later, the ΔPG recovery phase onset around 17:00 UT and slowly progressed to its fair weather range as shown in Figure 2e.

The phase of ΔPG is highly accompanied with overhead ionospheric potential as illustrated in Figures 5d and 5e, but the equivalent magnitude of ΔPG differs in some intervals. The uncertainty in the excess ΔPG (relative to the overhead ionospheric potential) should be addressed, so that the possibility of contributing various factors in the solar wind-magnetosphere coupling may be taken into consideration. The change of ΔPG may also possible by the energetic particle (electron and proton $>$ 10 MeV) precipitation over high-latitude ionosphere that alters the conductivity of upper atmosphere. This change in ionospheric conductivity substantially decreases/increases the vertical ionospheric potential (PG) [*Lobodin and Paramonov*, 1972; *Yeoman et al*., 2000; *Nikiforova et al*., 2005; *Kleimenova et al*., 2008].

On 17 March 2015, in Figure 7, PCP shows an increasing trend in morning hours 05:00–06:00 UT associated with a strong southward IMF ~-20 nT. In addition, IMF B_y shows a strong westward flow (-20 nT), which also modulates PCP by 100 kV during 06:00–07:00 UT. The dawn directed field lines with high-speed plasma motion and its equivalent electric field strengthen the negative potential region. In this situation, Vostok latitude is dominated by the negative potential region in all magnetic local time (MLT). It is expected to have strong influence of large-scale horizontal ionospheric electric field on *PG*; similarly, ΔPG shows gradual decreasing trend associated with downward trend (negative potential) of overhead potential as shown in Figure 7d. It can be observed from Figure 8a, the boundary of convection cell and HMB (Heppner-Maynard boundary proximity of the auroral oval location) extended toward lower latitude (~62°S magnetic latitude at dusk sector) as an effect of intense magnetic storm. It is apparent from ionospheric convection map that Vostok is under the influence of very intense negative potential region at 06:30 UT and extended till 07:00 UT. This negative potential region may lead to the change in phase of the downward mapping of ionospheric electric field on *PG* [*Roble and Hays*, 1979]. Therefore, the net effect substantially decreases ΔPG (-50 V/m) measured at ground level. Decreasing trend of ΔPG is gradually turned to increasing phase shortly after 08:00 UT, where IMF gradually turned toward the north and hence the strength of potential region is

decreased. It is noted that IMF B_y is still strongly negative, i.e., westward, which retains the negative potential region to remain active above Vostok. Even though, positive phase of ΔPG perhaps implies the weakening of convection cell, the influence of negative potential still persists over Vostok, which is also evident from time series of Weimer_05 potential as shown in Figure 7d. IMF gradually turns toward the north ($B_z > 0$) with the reduced plasma speed and density, which results in decreasing trend of PCP (30 kV). In this scenario, ΔPG supposed to get recovered from the prevailing magnetic disturbances, but it varied further negative by reaching -75 V/m at 10:20 UT, which is the lowest ΔPG observed during the entire period of observations on 17 March 2015. Supporting to the observation, Figures 8c and 8d depict the reduced effect of magnetic disturbances as ionospheric convection cell and its potential drop become weakens in the span of half an hour. In this scenario, under northward IMF, it is proposed that dusk cell (negative cell) occupies a larger area over a southern polar cap, single cell/single vortex, during strong westward IMF ($B_y < 0$) [*Crooker*, 1979; *Iijima et al*., 1984; *Lukianova et al*., 2011], which is evident from Figure 8d. *Akasofu and Chapman* [1972] and *Kamide* [1988] also reported that IMF confines the plasma motion within polar cap region for northward-westward IMF ($B_z > 0$ and $B_y < 0$), which is closely associated with space-time distribution of charged particle precipitations in the upper atmosphere. For $B_y \sim 0$, the pattern is symmetric. For $B_y < 0$, the dawn cell becomes circular and the dusk cell crescent-shaped, whereas for $B_y > 0$, the dusk cell becomes circular and dawn cell crescent-shaped in the Northern Hemisphere. In the Southern Hemisphere, for a given sign of B_y, the behavior of the cells is reversed**.** Time series of overhead potential highly supports the aforesaid inferences as Vostok is completely dominated by negative potential region, and its potential varied ~-30 kV, which is also nearly equivalent to the total polar cap potential drop (30 kV). This negative large-scale ionospheric electric field substantially superposed on Vostok *PG*. In this context, *Victor et al*. [2016] observed the similar situation, where Vostok PG changes -33% (relative to the quiet time curve) when IMF $B_y < 0$. However, the difference in magnitude of ΔPG to that of overhead potential is still noticeably high based on the linear relation [*Burns et al*., 2012].

The next course of IMF southward is occurred from 11:00 UT until the end of the day. It is noticed from Figure 7c that magnetic perturbation of B_z and B_y intensifies as high as -28 nT and +30 nT, respectively. The strong IMF southward leads for the high-dayside reconnection rate between the IMF and geomagnetic field, which in turn increase the electric field across dayside magnetopause that maps down the magnetic field lines to polar regions. At the ionospheric altitude, mapping of such electric field creates a plasma convection patterns between dawn and dusk, and the shape of the pattern is greatly controlled by the IMF B_y [*Heppner and Maynard*, 1987; *Rich and Hairston*, 1994; *Weimer*, 1995, 1996, 2001]. As explained above, in the GSM *Y-Z* plane, under southward IMF conditions, the dawnward directed magnetic field lines expand the area of the negative, clockwise, potential region, and duskward intensifies the anticlockwise, i.e., positive potential region. As shown in Figures 7d and 7e at 11:30 UT, overhead potential and ΔPG simultaneously increased, in which the potential enhances sharply due to the IMF fluctuations but the equivalent changes obscure on *PG*. This observation once again reveals that highly fluctuated ionospheric potential attenuates faster before it couples with *PG*, perhaps with lesser scale size (<500 km) [*Park*, 1976]. Ionospheric convection map obtained from SuperDARN, Figure 8e, also consistently show how the Vostok is merely dominated by the positive potential region. Later, ΔPG has a small decreasing trend followed by huge enhancement associated with the equivalent changes on overhead potential as shown in Figure 7. In the increasing phase of ΔPG 12:00–15:00 UT, two distinct peaks have been noticed, where the first peak (ΔPG = 60 V/m) coincides with overhead ionospheric potential (~65 kV) at 12:30 UT. It can be seen from Figure 7c, IMF B_y points highly positive, about 30 nT, around 13:00UT, which is the highest IMF B_y value registered during the entire period of observation. *Frank-Kamenetsky et al.* [2001] reported and *Lukianova et al.* [2011] agreed that when IMF $B_y > 0$ a tendency of increasing linear relation of Vostok *PG* with ionospheric potential, because IMF intensifies when a more powerful dawn convection vortex, positive potential region, develops in the southern polar cap. The later study further explained using LC06 model, in this scenario, Vostok trajectory passes below many equipotential lines, because of the change in ionospheric potential. As IMF B_y increases, the east-west flow superposes on the poleward drift and may be intensified by the appearance and development of oppositely directed sheets of field-aligned currents (FACs) in cusp regions. This FAC can augment strongly with the spatial-temporal asymmetry of the dayside PCP distribution [*Clauer et al.,* 1995; *Zakharov and Pudovkin*, 1996]. The combined effect dramatically increased the polar cap potential drop of >100 kV as seen in Figure 7a. The highest primary peak of ΔPG observed at 14:00 UT (ΔPG = 75 V/m) is due to successful

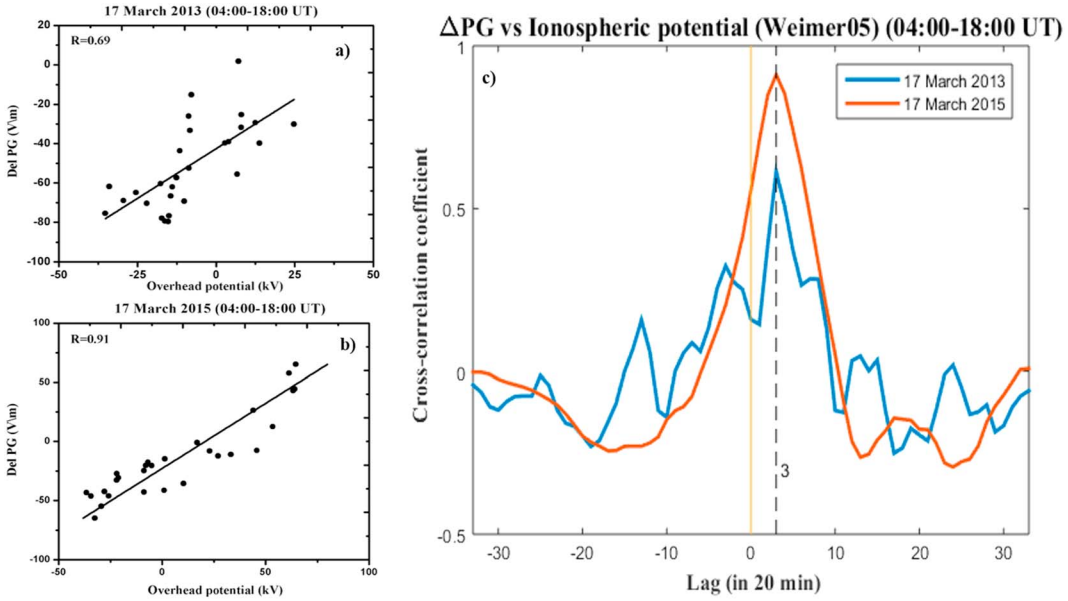

Figure 9. Linear regression analysis and cross correlation between ΔPG and ionospheric potential (Weimer_05) on 17 March 2013 and 17 March 2015.

downward mapping of a large-scale horizontal electric field. In this interval, IMF shows an intense southward trend (-25 nT at 13:30 UT) followed by large density blast ($>50/cm^3$) occurred around 13:00 UT as clearly seen from Figure 3. During this period (13:30 UT), highly positive B_y (~30 nT) along with the stable intense southward IMF intensified the positive potential region than former region (at 11:30 UT, IMF B_y = ~20 nT) as shown in Figure 8f, and Vostok is significantly dominated by this region. Interestingly, as seen from Figure 7, the attenuation factor is almost null as ~75 kV of ionospheric potential over Vostok significantly superpose on *PG* (ΔPG = 75 V/m). The rate at which *PG* varies with overhead potential is in good agreement with the range from 0.7 to 0.9 Vm^{-1} kV^{-1} [*Burns et al.*, 2012]. This observation is also evident for the chance of occurrences of one-to-one coupling between *PG* and ionospheric potential under some extraordinary circumstances [*Tinsley et al.*, 1998].

Shortly later at 14:30 UT, ΔPG starts to decrease gradually with overhead potential, then ΔPG crossed null value and continued to highly negative value of -50 V/m whereas overhead potential ended up with a reference line (~0 kV) around 16:00UT. It can be observed from Figure 3d, the plasma density abruptly increased by a sharp lift from $20/cm^3$ to $>40/cm^3$, which is strongly aligned with southward IMF ($B_z = -22$ nT and $B_y = -10$ nT) around 16:00 UT. As discussed above, the westward IMF substantially intensifies the negative potential region at above Vostok latitude; in addition, the strong southward IMF is also strengthening this process. As a result, in this situation, the enhanced ionospheric potential of -58 kV (inferred from SuperDARN) superposed on *PG* at Vostok. Noteworthy, the nightside boundary of the convection cell is moving and variable during this period compared to the stability of the dayside boundary [*Hairston et al.*, 2016]. Figure 9 represents the linear regression analysis and cross correlation between ΔPG and ionospheric potential on 17 March 2013 and 17 March 2015. The regression coefficient (R) between half-hourly *PG* and ionospheric potential is highly significant ~0.91 on 17 March 2015, and for 17 March 2013 the link is relatively important, $R = 0.69$, as seen in Figures 9a and 9b. The time lag (60 min) found in Figure 9c, marked by a dotted line, is the delay in response of Vostok *PG* to change of ionospheric potential. The smooth curve with higher coefficient (CCF = 0.91) on 17 March 2015 may be referred the steady sate variation of SW-IMF, whereas the curve on 17 March 2013 (CCF = 0.65) likely due to the fluctuation of SW-IMF.

On 17 March 2015, the relation between Vostok ΔPG and modeled overhead potential is highly positive during noon hours (10:00–15:00 UT) and degraded for morning and evening sectors. These observational inferences are highly consistent with earlier studies [*Frank-Kamenetsky et al.*, 1999; *Lukianova et al.*, 2011; *Frank-Kamenetsky et al.*, 2012], which state that significant control of ionospheric convection pattern and its associated electric field ($V_{sw} \times B$) by IMF parameters is more efficient during noon hours (magnetic day

time) [*Victor et al*., 2016]. In addition, a statistical analysis using Vostok *PG* by *Burns et al.* [2005, 2012] was also reported that the standard error on the association between *PG* and overhead ionospheric potential (Weimer_96, Weimer_2001 and Weimer_01, and *AL* model) is less ($<$0.2 Vm^{-1} per kV) during 08:00–16:00 UT, where the lowest error was estimated near noon hours at Vostok. He further quantified the slope between Vostok *PG* and overhead potential is considerably high during noon hours ~1.0 Vm^{-1} per kV (March), which is closely matching with our noon time *PG* observation on 17 March 2015. The evening sector (UT and MLT) is contaminated by magnetotail energy input to the high-latitude ionosphere, which in turn trigger the asymmetric nature of ionospheric convection cell and its associated potential during magnetic storm [*Michnowski*, 1998]. Moreover, this kind of local changes would not be described in the global convection models. Therefore, the close association between Vostok *PG* and overhead ionospheric potential may be feeble during dusk hours. Time series of ionospheric potential obtained from Weimer_05 is in good agreement with southern polar cap potential drop that derived from DMSP satellite (F19) [*Hairston et al*., 2016]. The maximum potential drop occurred during 12:00–14:00 UT is good agreement with Weimer_05 model and SuperDARN as well. In addition, the ionospheric potential obtained from the Weimer model is also consistent with the electric potential of ionosphere by SuperDARN map potential technique [*Kubicki et al*., 2014].

Similarly, the ΔPG variation on 17 March 2013 coincided with Weimer modeled overhead potential from 08:00 UT to 14:00 UT. However, the association in terms of magnitude of ΔPG to that of overhead potential (Weimer_05 model) is slightly less significant. As discussed in previous sections, solar wind and IMF are highly fluctuating due to turbulent motion of solar wind plasma, which perhaps leads to an inconsistency in transferring magnetospheric electric field to the ionosphere. However, the observation demonstrates that largest negative values of ΔPG correspond to the closest vicinity of strong negative potential region which occupies the entire polar region when IMF $B_y \ll 0$. These kind observations may lead to an estimation of limitations between model and radar observation. It is also inferred from Figures 5d, 5e, 7d, and 7e that the steady changes of SW-IMF parameters lead for the better association of *PG* with ionospheric potential.

On an average, it is noticeable from Figures 2e and 4e that the observed diurnal variation of *PG* is significantly departed from quiet time curve (PGQ) during geomagnetic activity. The difference in magnitude as depicted in Figures 5d and 7d varies from +20 to −85 V/m (*Kp* = 7) on 17 March 2013 and −75 V/m to +75 V/m (56%, *Kp* = 8) on 17 March 2015, which are good agreement with the numerical model output of 30–100% changes estimated on ΔPG with respect to change in ionospheric potential [*Park*, 1976; *Michnowski*, 1998] and observed at middle latitude 30–50% [*Ptitsyna et al*., 1997], and at polar cap, Vostok, 61% (*Kp* = 8) [*Victor et al*., 2016]. The present observations also demonstrate that Vostok *PG* decreased (increased) when it is under negative (positive) potential region during geomagnetic perturbation. This observation strengthens the earlier studies, which state that downward mapping of large-scale ionospheric electric field is in phase (positive coupling) with global thunderstorm-generated electric field (*PG*) when the station is dominated by positive potential region. As a counterpart, the negative potential region may lead to the negative coupling, since the mapping field antiphase with prevailing vertical electric field [*Panneerselvam et al*., 2010; *Lukianova et al*., 2011; *Kleimenova et al*., 2013].

Apart from the aforesaid dominating factors of solar wind-magnetosphere-ionosphere-atmosphere coupling, a few other factors may also play a vital role in this context, (a) the scale size of the ionospheric electric field as suggested by *Park* [1976], which is expected to be larger in (scale) size ($>$500 km) so that the field will map to the ground level without much attenuation due to the conductivity profile, otherwise it may rapidly attenuate and vanish before it reaches the surface. It is still puzzle to determine the scale size of the ionospheric electric field at ionospheric altitude; (b) *Tonev and Velinov*, [2011] suggested that the downward coupling would have been associated with the small residual part of FAC due to their incomplete closure in the dynamo region. *Frank-Kamenetsky et al.* [2012] have also quantitatively reported that FACs play a considerable role in the discussion of the current system for the corresponding relation between ΔPG at auroral region and overhead potential. However, at present study, the linear regression analysis implies that the contribution of overhead potential is almost 91% on 17 March 2015 and 69% on 17 March 2013, and hence, the contribution percentage of FAC is not rigorously considered here, though the value is not negligible.

Hence, there is a missing link between the association between solar wind-magnetosphere interaction and its associated changes in vertical ionospheric potential (*PG*), which is yet to be clearly understood. The effects of different combinations of the IMF components on the ionospheric convection pattern, which in turn couple

to *PG* in a different manner, deserve more observation and analysis on the transient space weather events to climatology scale.

4. Conclusion

We have investigated the influence of solar wind-magnetospheric interaction and its associated ionospheric electric field impact on ground level potential gradient at Vostok. Diurnal variation of Vostok *PG* on two severe geomagnetic storms (*Kp* = 8) distinctly represents the storm time signatures manifested by magnetosphere-ionosphere-atmosphere coupling. A traditional method has been adopted to distinguish the global thunderstorm electric field and magnetospheric contribution from *PG* measurement. During geomagnetic storms, overhead ionospheric potential, obtained from the Weimer_05 model, significantly coupled with *PG* variation. Eventually, for the first time, the slope of ~1.0 Vm^{-1} per kV has been demonstrated between Vostok *PG* and its overhead ionospheric potential (model) during very intense geomagnetic perturbation (*Kp* = 8). The linear relation between Vostok *PG* and solar wind-IMF-imposed potential is highly pronounced during positive coupling (*PG* is relatively higher than PGQ) on 17 March 2015, whereas, for negative coupling, the relation is descended in terms of amplitude. Similarly, the relation is also less compatible with drastic changes of overhead potential due to a strong fluctuation of IMF resulting from the turbulent motion of solar wind plasma on 17 March 2013. However, it is found that the phase of ionospheric potential is highly consistent with ΔPG on both types of coupling. Cross correlation signifies the time delay of ~60 min between ΔPG and ionospheric potential. The ionospheric convection map obtained from SuperDARN radar significantly represents ionospheric potential region relative to the Vostok latitude. The largest negative changes of ΔPG mostly occurred when the single negative convection pattern occupied the entire polar cap due to the strong westward motion of IMF (IMF $B_y \ll 0$). In such cases, consistency between radar and model is highly pronounced but their amplitude is less accountable on ΔPG.

Therefore, it is inferred that Weimer_05 model and SuperDARN radar convection map are self-consistent with Vostok *PG*, when it is under the positive potential region, whereas the negative changes of *PG* have offset of ~25 V/m with an empirical model. The uncertainty in the amplitude on negative coupling may be due to modulation of ionospheric conductivity which is owing to the particle precipitation over upper atmosphere. The study also demonstrates that Vostok *PG* is highly sensitive to the overhead potential for steady variation of solar wind and IMF components, whereas the relation is less significant for rapid changes of SW-IMF parameters. It is thought to be due to fast-varying potential which attenuates faster than steady state variation; the later field perhaps has large-scale size (>300 km). However, similar kind of observations is needed to further establish the link between the rate of change of IMF and its associated ionospheric potential superposed on the atmospheric electric field.

Therefore, it is necessary to study the impact of each geomagnetic storm and its associated high-latitude perturbation on the atmospheric electric field in conjunction with SW-IMF changes in the wide network of stations to investigate the complexity involved in solar-terrestrial coupling.

Acknowledgments

The authors are grateful to D.S. Ramesh, Director, IIG, for giving permission to publish this work. The authors express their gratitude to the Department of Science and Technology (DST), India. We thank Kyoto WDC (http://wdc.kugi.kyoto-u.ac.jp/) for the *SYM-H*, *AL*, *AU*, and *Kp* data and Wind satellite team for the CME and IMF data (http://omniweb.gsfc.nasa.gov/). The electric field mills deployed at Vostok was developed under Australian Antarctic Science Advisory Committee Project 974. Llyod Symons, Australian Antarctic and data division, developed the electric field mill electronics and data collection software. The data for Vostok obtained from Arctic and Antarctic Research Institute (http://www.geophys.aari.ru/index.html). The results presented in this paper rely on the data collected at Vostok, Antarctica, and SuperDARN data. We thank the national scientific funding agencies of Australia, Canada, China, France, Italy, Japan, South Africa, UK, and USA that funded the radars of the SuperDARN network. We also thank Kleimenova and other referees for their constructive comments and revision of this manuscript.

References

Akasofu, S.-I., and S. Chapman (1972), *Solar-Terrestrial Physics*, p. 624, Oxford Univ. Press, New York.

Alderman, E. J., and E. R. Williams (1996), Seasonal variation of the global electric circuit, *J. Geophys. Res.*, *101*, 29,679–29,688, doi:10.1029/96JD01547.

Apsen, A. G., K. D. Kanonidi, S. P. Chernyshova, D. N. Chetaev, and V. M. Sheftel (1988), *Magnetospheric Effects in Atmospheric Electricity*, Nauka, Moscow.

Aruliah, A. L., A. D. Farmer, T. J. Fuller-Rowell, M. N. Wild, M. Hapgood, and D. Rees (1996), An equinoctial asymmetry in the high-latitude thermosphere and ionosphere, *J. Geophys. Res.*, *101*(A7), 15,713–15,722, doi:10.1029/95JA01102.

Belova, E., S. Kirkwood, and H. Tammet (2001), The effect of magnetic substorms on near-ground atmospheric currents, *Ann. Geophys.*, *18*, 1623–1629, doi:10.1007/s00585-001-1623-z.

Bering, E. A., III, A. A. Few, and J. R. Benbrook (1998), The global electric circuit, *Phys. Today*, *51*, 24–30.

Boyle, C. B., P. H. Reiff, and M. R. Hairston (1997), Empirical polar cap potentials, *J. Geophys. Res.*, *102*(A1), 111–125, doi:10.1029/96JA01742.

Burns, G. B., A. V. Frank-Kamenetsky, O. A. Troshichev, E. A. Bering, and B. D. Reddell (2005), Inter-annual consistency of bi-monthly differences in diurnal variations of the ground-level, vertical electric field, *J. Geophys. Res.*, *110*, D10106, doi:10.1029/2004JD005469.

Burns, G. B., A. Tinsley, A. V. Frank-Kamenetsky, O. A. Troshichev, W. J. R. French, and R. Klekociuk (2012), Monthly diurnal global atmospheric circuit estimates derived from Vostok electric field measurements adjusted for local meteorological and solar wind influences, *J. Atmos. Sci.*, *69*, 2061–2082, doi:10.1175/JAS-D-11-0212.1.

Böstrom, R., and U. Fahleson (1977), Vertical propagation of time dependent electric fields in the atmosphere and ionosphere, in *Electrical Processes in Atmospheres*, edited by H. Dolezalek and R. Reiter, pp. 529–530, Steinkopff, Darmstadt, Germany.

Clauer, C. R., P. Stauning, T. J. Rosenberg, E. Friis-Christensen, P. M. Miller, and R. J. Sitar (1995), Observations of a solar-wind-driven modulation of the dayside ionospheric DPY current system, *J. Geophys. Res.*, *100*(A5), 7697–7713, doi:10.1029/94JA01193.

Corney, R. C., G. B. Burns, K. Michael, A. V. Frank-Kamenetsky, O. A. Troshichev, E. A. Bering, V. O. Papitashvili, A. M. Breed, and M. L. Duldig (2003), The influence of polar-cap convection on the geoelectric field at Vostok, Antarctica, *J. Atmos. Sol. Terr. Phys.*, *65*, 345–357.

Crooker, N. U. (1979), Dayside merging and cusp geometry, *J. Geophys. Res.*, *84*(A3), 951–959, doi:10.1029/JA084iA03p00951.

De Michelis, P., G. Consolini, R. Tozzi, and M. F. Marcucci (2016), Observations of high-latitude geomagnetic field fluctuations during St. Patrick's Day storm: Swarm and SuperDARN measurements, *Earth Planets Space*, *68*, 105, doi:10.1186/s40623-016-0476-3.

Frank-Kamenetsky, A. V., G. B. Bums, O. A. Troshichev, V. O. Papitashvili, E. A. Bering, and W. J. R. French (1999), The geoelectric field at Vostok, Antarctica: Its relation to the interplanetary magnetic field and the cross polar cap potential difference, *J. Atmos. Sol. Terr. Phys.*, *61*, 1347.

Frank-Kamenetsky, A. V., O. A. Troshichev, G. B. Burns, and V. O. Papitashvili (2001), Variations of the atmospheric electric field in the near-pole region related to the interplanetary magnetic field, *J. Geophys. Res.*, *106A*, 179–190, doi:10.1029/2000JA900058.

Frank-Kamenetsky, A., A. Kotikov, A. Kruglov, B. Burns, N. Kleimenova, O. Kozyreva, M. Kubitski, and A. Odzimek (2012), Variations in the near-surface atmospheric electric field at high latitudes and ionospheric potential during geomagnetic perturbations, *Geomagn. Aeron.*, *5*, 629–638.

Galperin, Y. I., V. N. Ponomarev, and A. G. Zosimova (1978), Equatorial ionospheric anomaly and interplanetary magnetic field, *J. Geophys. Res.*, *83*(A9), 4265–4272, doi:10.1029/JA083iA09p04265.

Gao, Y., M. G. Kivelson, and R. J. Walker (2013), Two models of cross polar cap potential saturation compared: Siscoe-Hill model versus Kivelson-Ridley model, *J. Geophys. Res. Space Physics*, *118*, 794–803, doi:10.1002/jgra.50124.

Hairston, M. R., and R. A. Heelis (1995), Response time of the polar ionospheric convection pattern to changes in the north-south direction of the IMF, *Geophys. Res. Lett.*, *22*, 631–634, doi:10.1029/94GL03385.

Hairston, M., W. R. Coley, and R. Stoneback (2016), Responses in the polar and equatorial ionosphere to the March 2015 St. Patrick Day storm, *J. Geophys. Res. Space Physics*, *121*, 11,213–11,234, doi:10.1002/2016JA023165.

Hashimoto, K. K., and T. Kikuchi (2005), Quick response of the near-Earth magnetotail to changes in the interplanetary magnetic field, in *The Inner Magnetosphere: Physics and Modeling*, *Geophys. Monogr. Ser.*, vol. 155, edited by T. I. Pulkkinen, N. A. Tsyganenko, and R. H. W. Friedel, pp. 47–53, AGU, Washington, D. C., doi:10.1029/155GM06.

Heelis, R. A. (1978), Ionospheric convection at high latitudes, in *Magnetospheric Boundary Layers*, ESA SP-148, pp. 175–181, ESTEC, Noordwijk, Netherlands.

Heppner, J. P., and N. C. Maynard (1987), Empirical high-latitude electric field models, *J. Geophys. Res.*, *92*, 4467–4489, doi:10.1029/JA092iA05p04467.

Iijima, T., J. S. Kim, and M. Sugiura (1984), A case-study of the evolution of polar-cap currents and auroral electrojets during polar geomagnetic disturbances with IMS magnetometer data, *Geophys. J. Int.*, *77*(3), 729–752, doi:10.1111/j.1365-246X.1984.tb02218.x.

Kamide, Y. (1988), *Electrodynamic Processes in the Earth's Ionosphere and Magnetosphere*, 785 pp., Kyoto Sangyo Univ. Press, Kyoto.

Kantelhardt, J. W., S. A. Zschiegner, E. Koscielny-Bunde, A. Bunde, S. Havlin, and H. E. Stanley (2002), Multifractal detrended fluctuation analysis of nonstationary time series, *Phys. A*, *316*(1–4), 87–114.

Khan, H., and S. W. H. Cowley (2001), Effect of the IMF by component on the ionospheric flow overhead at EISCAT: Observations and theory, *Ann. Geophys.*, *18*, 1503–1522.

Kleimenova, N. G., O. V. Kozyreva, N. N. Nikiforova, S. Michnowski, and M. Kubicki (2006), Atmospheric electric field variations at polar latitudes (Obs. Hornsund, Spitsbergen), Proc. 3rd Int. Conf. "Geophysical Research in Spitsbergen Archipelago", Barentsburg, pp. 11–19.

Kleimenova, N. G., O. V. Kozyreva, S. Michnowski, and M. Kubicki (2008), Effect of magnetic storms in variations in the atmospheric electric field at midlatitudes, *Geomagn. Aeron.*, *48*(5), 622–630.

Kleimenova, N. G., O. V. Kozyreva, M. Kubicki, and S. Michnowski (2010), Morning polar substorms and variations in the atmospheric electric field, *Geomagn. Aeron.*, *50*, 48–57.

Kleimenova, N. G., O. Kozyreva, M. Kubicki, A. Odzimek, and L. Malysheva (2012), Effect of substorms in the Earth's nightside sector on variations in the surface atmospheric electric field at polar and equatorial latitudes, *Geomagn. Aeron.*, *52*, 467–473.

Kleimenova, N. G., O. V. Kozyreva, S. Michnowski, and M. Kubicki (2013), Influence of geomagnetic disturbances on atmospheric electric field (Ez) variations at high and middle latitudes, *J. Atmos. Sol. Terr. Phys.*, *99*, 117–122.

Kozyreva, O. V., N. N. Nikiforova, N. G. Kleimenova, S. Michnowski, and M. Kubicki (2007), Electric air-Earth vertical current pulsations at Hornsund during polar substorms: Case study, in *Proc. 13th Int. Conf. on Atmospheric Electricity (ICAE)*, pp. 29–33, Beijing.

Kruglov, A. A., A. V. Frank-Kamenetsky, G. B. Burns, J. French, and V. N. Morozov (2010), On the connection between variations of atmospheric electric field as measured at ground surface in the Central Antarctica and ionospheric potential, in *Proc. 33rd Annual Seminar "Physics of Auroral Phenomena"*, pp. 171–174, Apatity, Russia.

Kubicki, M., A. Odzimek, N. G. Kleimenova, O. V. Kozyreva, and M. Neska (2014), Synchronization of main global electric circuit generators from ground-level electric field Ez at three distant locations on the globe at middle and high latitudes, in *Proc. 15th Int. Conf. on Atmospheric Electricity*, 9 pp., Norman, Okla., 15–20 June.

Lobodin, T. V., and N. A. Paramonov (1972), Variations of atmospheric-electric field during aurorae, *Pure Appl. Geophys.*, *100*, 167–173.

Lukianova, R. Y., A. A. Kruglov, A. V. Frank-Kamenetskii, A. L. Kotikov, G. B. Burns, and V. D. R. French (2011), Relationship between the ionospheric potential and the ground-level electric field in the southern polar cap, *Geomagn. Aeron.*, *51*, 383–393.

Markson, R. (2007), The global circuit intensity: Its measurement and variation over the last 50 years, *Bull. Am. Meteorol. Soc.*, 223–241, doi:10.1175/BAMS-88-2-223.

Michnowski, S. (1991), Concluding remarks on the Madralin Workshop, in *Proc. Int. Workshop on Global Atmospheric Electricity Measurements*, *Publ. Inst. Geophys. Pol. Acad. Sci.*, D-35, 238.

Michnowski, S. (1998), Solar wind influences on atmospheric electricity variables in polar regions, *J. Geophys. Res.*, *103*, 13,939–13,948, doi:10.1029/98JD01312.

Michnowski, S., A. Odzimek, N. G. Kleimenova, O. V. Kozyreva, M. Kubicki, and N. N. Nikiforova (2014), Review of examples of solar wind lower atmosphere coupling observed in the electric field (Ez) variations at the Earth's surface during magnetic storms, in *Proc. 15th Int. Conf. on Atmospheric Electricity*, Norman, Okla., 15–20 June.

Morozov, V. N., and O. A. Troshichev (2008), Simulation of variations in the polar atmospheric electric field related to the magnetospheric field-aligned currents, *Geomagn. Aeron.*, *48*, 727–736.

Nikiforova, N. N., N. G. Kleimenova, O. V. Kozyreva, M. Kubicki, and S. Michnowski (2003), Influence of auroral-latitude precipitation of energetic electrons on variations in the atmospheric electric field at polar latitudes (Spitsbergen Archipelago), *Geomagn. Aeron.*, *43*, 29–35.

Nikiforova, N. N., N. G. Kleimenova, O. V. Kozyreva, M. Kubitski, and S. Michnowski (2005), Unusual variations in the atmospheric electric field during the main phase of the strong magnetic storm of October 30, 2003, at Swider polish mid-latitude observatory, *Geomagn. Aeron.*, *45*(1), 140–144.

Odzimek, A., M. Kubicki, M. Lester, and A. Grocott (2011), Relation between SuperDARN ionospheric potential and ground electric field at Polar Station Hornsund, in *Proc. 14th Int. Conf. on Atmospheric Electricity*, 4 pp., Rio de Janeiro, Brazil, 7–12 Aug.

Panneerselvam, C., C. P. Anil Kumar, D. Ajay, K. U. Nair, C. Selvaraj, S. Gurubaran, and B. M. Pathan (2010), Instrumentation for the surface measurements of atmospheric electrical parameters at Maitri, Antarctica: First results, *Earth Planets Space*, *62*, 545–549.

Papitashvili, V. O., B. A. Belov, D. S. Faermark, Y. I. Feldstein, S. A. Golyshev, L. I. Gromova, and A. E. Levitin (1994), Electric potential patterns in the northern and southern polar regions parameterized by the inter-planetary magnetic field, *J. Geophys. Res.*, *99*, 13,251–13,262, doi:10.1029/94JA00822.

Park, C. G. (1976), Downward mapping of high-latitude ionospheric electric fields to the ground, *J. Geophys. Res.*, *81*, 168–174, doi:10.1029/JA081i001p00168.

Ptitsyna, N., T. J. Tuomi, A. Levitin, and I. Gromova (1997), Magnetospheric—Ionospheric effect on the ground-level atmospheric electric field at Helsinki, *J. Atmos. Sol. Terr. Phys.*, *59*(I), 99–105.

Richmond, A. D. (1986), Upper-atmosphere electric-field sources, in *The Earth's Electrical Environment (Studies in Geophysics)*, pp. 195–205, Natl. Res. Council, Wash.

Rich, J. R., and H. Hairston (1994), Large-scale convection patterns observed by DMSP, *J. Geophys. Res.*, *99*, 3827–3844, doi:10.1029/93JA03296.

Ridley, A. J., G. Lu, C. R. Clauer, and V. O. Papitashvili (1998), A statistical study of the ionospheric convection response to changing interplanetary magnetic field conditions using the assimilative mapping of ionospheric dynamics technique, *J. Geophys. Res.*, *103*, 4023–4039, doi:10.1029/97JA03328.

Roble, R. G., and R. B. Hays (1979), A quasi-static model of global atmospheric electricity 2. Electrical coupling between the upper and lower atmosphere, *J. Geophys. Res.*, *84*, 7247–7256, doi:10.1029/JA084iA12p07247.

Roble, R. G., and I. Tzur (1986), The global atmospheric-electrical circuit, in *The Earth's Electrical Environment*, *Studies in Geophysics*, pp. 206–231, Natl. Acad., Wash.

Ruohoniemi, J. M., and R. A. Greenwald (2005), Dependencies of high-latitude plasma convection: Consideration of IMF, seasonal, and UT factors in statistical patterns, *J. Geophys. Res.*, *110*, A09204, doi:10.1029/2004JA010815.

Rycroft, M. J., and R. G. Harrison, (2011), Electromagnetic atmosphere-plasma coupling: The global atmospheric electric circuit, *Space Sci. Rev.*, *1–22*, doi:10.1007/s11214-011-9830-8.

Rycroft, M. J., Keri A. Nicoll, Karen L. Aplin, and R. Giles Harrison (2012), Recent advances in global electric circuit coupling between the space environment and the troposphere, *J. Atmos. Sol. Terr. Phys.*, *90–91*, 198–211, doi:10.1016/j.jastp.2012.03.015.

Sheftel, V. M., O. I. Bandilet, A. N. Yaroshenko, and A. K. Chernyshev (1994), Space time structure and reasons of global, regional, and local variations of atmospheric electricity, *J. Geophys. Res.*, *99*, 10,797–10,806, doi:10.1029/93JD02857.

Tinsley, B. A. (2000), Influence of solar wind on the global electric circuit, and inferred effects on cloud microphysics, temperature and dynamics in the troposphere, *Space Sci. Rev.*, *94*, 231–258.

Tinsley, B. A., and R. A. Heelis (1993), Correlation of atmospheric dynamics with solar activity: Evidence for a connection via the solar wind, atmospheric electricity, and cloud microphysics, *J. Geophys. Res.*, *98*, 10,375–10,384, doi:10.1029/93JD00627.

Tinsley, B. A., W. Liu, and R. P. Rohrbaugh (1998), South Pole electric field responses to overhead ionospheric convection, *J. Geophys. Res.*, *103*, 26,137–26,146, doi:10.1029/98JD02646.

Tonev, P. T., and P. I. Y. Velinov (2011), Model study of the influence of solar wind parameters on electric currents and fields in middle atmosphere at high latitudes, *Explor. Cosmiques (Bulgarian Acad. Sci.)*, *64*(12), 1733–1742.

Victor, N. J., S. Manu, A. V. Frank-Kamenetsky, C. Panneerselvam, C. P. Anil Kumar, and P. Elango (2016), Network of observations on the atmospheric electrical parameters during geomagnetic storm on 5 April 2010, *J. Geophys. Res. Space Physics*, *121*, 2407–2417, doi:10.1002/2015JA022080.

Weimer, D. R. (1995), Models of high-latitude electric potentials derived with a least error fit of spherical harmonic coefficients, *J. Geophys. Res.*, *100*, 19,595–19,607, doi:10.1029/95JA01755.

Weimer, D. R. (1996), A flexible, IMF dependent model of high-latitude electric potentials having "space weather" applications, *Geophys. Res. Lett.*, *23*, 2549–2552, doi:10.1029/96GL02255.

Weimer, D. R. (2000),A new technique for the mapping of ionospheric field-aligned currents from satellite magnetometer data, in *Magnetospheric Current Systems*, edited by S.-I. Ohtani, et al., pp. 381–388, AGU, Washington, D. C., doi:10.1029/GM118p0381.

Weimer, D. R. (2001), An improved model of ionospheric electric potentials including substorm perturbations and application to the geospace environment modelling November 24, 1996, event, *J. Geophys. Res.*, *106*, 407–416, doi:10.1029/2000JA000604.

Weimer, D. R. (2005a), Improved ionospheric electrodynamic models and application to calculating Joule heating rates, *J. Geophys. Res.*, *110*, A05306, doi:10.1029/2004JA010884.

Weimer, D. R. (2005b), Predicting surface geomagnetic variations using ionospheric electrodynamic models, *J. Geophys. Res.*, *110*, A12307, doi:10.1029/2005JA011270.

Wilson, C. T. R. (1925), The electric field of the thundercloud and some of its effects, *Proc. Phys. Soc. London Sec. A*, *111*, 32D.

Yeoman, T. K., J. A. Davies, N. M. Wade, G. Provan, and S. E. Milan (2000), Combined CUTLASS, EISCAT and ESR observations of ionospheric plasma flows at the onset of an isolated substorm, *Ann. Geophys.*, *18*, 1073–1087.

Zakharov, V. E., and M. I. Pudovkin (1996), Electrodynamic coupling between ionospheric patterns in the Northern and Southern Hemispheres, *Ann. Geophys.*, *14*, 419–430.